



CHORUS

This is the accepted manuscript made available via CHORUS. The article has been published as:

Oxidation-Mediated Fingering in Liquid Metals

Collin B. Eaker, David C. Hight, John D. O'Regan, Michael D. Dickey, and Karen E. Daniels

Phys. Rev. Lett. **119**, 174502 — Published 27 October 2017

DOI: [10.1103/PhysRevLett.119.174502](https://doi.org/10.1103/PhysRevLett.119.174502)

Oxidation-Mediated Fingering in Liquid Metals

Collin B. Eaker¹, David C. Hight¹, John D. O'Regan¹, Michael D. Dickey¹, Karen E. Daniels²

¹*Dept. of Chemical and Biomolecular Engineering, North Carolina State University, Raleigh, NC, USA* ²*Dept. of Physics, North Carolina State University, Raleigh, NC, USA*

(Dated: September 19, 2017)

We identify and characterize a new class of fingering instabilities in liquid metals; these instabilities are unexpected due to the large interfacial tension of metals. Electrochemical oxidation lowers the effective interfacial tension of a gallium-based liquid metal alloy to values approaching zero, thereby inducing drastic shape changes, including the formation of fractals. The measured fractal dimension ($D = 1.3 \pm 0.05$) places the instability in a different universality class than other fingering instabilities. By characterizing changes in morphology and dynamics as a function of droplet volume and applied electric potential, we identify the three main forces involved in this process: interfacial tension, gravity, and oxidative stress. Importantly, we find that electrochemical oxidation can generate compressive interfacial forces that oppose the tensile forces at a liquid interface. Thus, the surface oxide layer not only induces instabilities, but ultimately provides a physical and electrochemical barrier that halts the instabilities at larger positive potentials. Controlling the competition between interfacial tension and oxidative (compressive) stresses at the interface is important for the development of reconfigurable electronic, electromagnetic, and optical devices that take advantage of the metallic properties of liquid metals.

PACS numbers: 47.53.+n, 47.20.Dr 81.65.Mq

Fingering patterns arise via a number of different spreading mechanisms: viscous fingering and diffusion limited aggregation [1–5], directional solidification [6, 7], Marangoni-driven spreading [8, 9], zero-surface-tension granular [10] and ordinary [11] fluids, bacterial colony growth [12], and Lichtenberg figures created by dielectric breakdown [13]. Liquid metals have many potential applications [14–20] due to their thermal, optical, and electrical properties but, with the largest surface tension of any known room-temperature fluid, they are both difficult to spread and an unlikely candidate to undergo fingering instabilities. Here, we demonstrate a novel fingering mechanism by which liquid metals form branched, lobed structures via electrochemical surface oxidation, and identify that compressive oxidative stresses (opposing the interfacial tension) play a key role in the destabilization.

This study focuses on eutectic gallium indium (EGaIn, from Indium Corp.), a room temperature liquid metal that offers a low-toxicity alternative to mercury. Although a native oxide forms spontaneously and rapidly on EGaIn in the presence of air, acidic or alkaline electrolytes remove the oxide and leave the bare metal in a state of large interfacial tension ($\gamma \approx 500$ mN/m). Applying potentials $\mathcal{E} > 0.2$ V to the metal in these solutions causes electrochemical deposition of a surface-active oxide that lowers γ [21, 22]. The dissolution of the oxide by the electrolyte competes with the electrochemical deposition of the oxide, thereby allowing the metal to maintain fluidity at low potentials, despite the presence of the oxide. Consequently, droplets of metal assume a shape arising from the balance between interfacial tension and gravity. Increasing \mathcal{E} drives surface oxidation, creating compressive stress that lowers the effective interfacial tension sufficiently to permit fingering instabilities. However, at sufficiently high \mathcal{E} , the oxide thickens and provides both a resistive and mechanical barrier that suppresses the growth of instabilities. Thus, the same oxide which destabilizes the droplet ultimately suppresses these instabilities.

Figure 1a shows a sample fractal morphology observed at

intermediate potentials. The initially spherical drop becomes increasingly branched as it spreads outwards, with length scales spanning several orders of magnitude. The droplet reaches a maximum surface area as the branches of the liquid metal become so thin that they pinch off from the main droplet. (Movies are available in the Supp. Mat.) Although this spreading process appears superficially similar to viscous fingering in a Hele-Shaw geometry [23, 24], there are numerous distinguishing characteristics. First, the measured fractal dimension ($D = 1.30 \pm 0.05$) is smaller than the value observed in viscous fingering ($D = 1.7$), indicating that this system belongs to a different universality class. Second, whereas viscous fingering typically occurs when injecting fluid at constant flux or pressure, the instabilities here occur for an unconfined, constant-volume droplet. Finally, viscous fingering occurs in the less viscous of the two fluids; here, EGaIn is approximately twice as viscous as the surrounding fluid. In this paper, we identify the novel mechanisms behind this new instability as arising due to interfacial tension, gravity, and oxidative stress. The last effect is the most noteworthy because interfacial forces are typically in tension, but here we show that electrochemical oxidation offers a way to create opposing forces (compression; equivalently, a negative contribution to the interfacial tension) that can overcome interfacial tension and help drive instabilities. We explore the different morphologies observed, explain the phase boundaries between them, and identify a scaling collapse for droplets of different sizes that shows larger droplets require larger potentials to suppress instabilities.

Experiments: The apparatus consists of a shallow dish filled with 1 M sodium hydroxide (NaOH) solution to provide active dissolution of the oxide layer and increase the ionic strength relative to de-ionized water. The outer rim of the apparatus contains a copper ring electrode, with an inner radius of 7.6 cm and outer radius of 8.6 cm, centered around the EGaIn droplet placed on the central working electrode (see Fig. 1a). We vary two parameters: the volume V of the

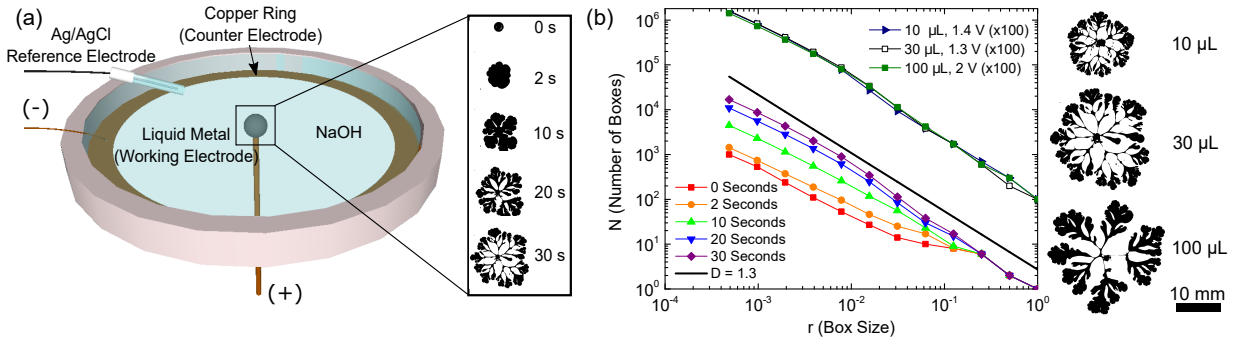


FIG. 1: (a) Schematic of apparatus, and experimental images of a $30 \mu\text{L}$ EGaIn droplet undergoing the fingering instability (see Movies 1-4). (b) Box-counting plot shown as a function of time for this same droplet, spreading at 1.3 V. The upper curves are box-counting plots for droplets with $V = 10 \mu\text{L}$, $30 \mu\text{L}$, and $100 \mu\text{L}$ (see images), both analyzed immediately before the first branch breaks off.

droplet and applied potential \mathcal{E} . All measurements utilize a saturated silver/silver-chloride (Ag/AgCl) reference electrode placed within the NaOH solution. For this system, the potential at open circuit is -1.5 ± 0.005 V vs. Ag/AgCl. Therefore, all reported potentials are calculated relative to this open circuit (i.e. adding 1.5 V to the measured value). During each run, we fix \mathcal{E} and monitor the current $I(t)$ with a Gamry potentiostat (resolution $\pm 0.2\%$). Leveling the apparatus eliminates gravitational gradients, and an overhead video camera records a cross-sectional image of the droplet at 30 Hz. We measure the droplet area $A(t)$ by thresholding the image at half the maximum grayscale value; We find the thresholding error to be negligible in all cases. We perform a total of 365 trials spanning 4 droplet volumes ($V = 3, 10, 30, 100 \mu\text{L}$) and a range of electric potentials $0.7 \text{ V} < \mathcal{E} < 5.5 \text{ V}$. To prevent undesired changes in droplet composition due to gallium dissolution into the fluid, we typically use a new droplet for each \mathcal{E} -series of measurements, and new solution for each V -series.

Fractal dimension: To quantify the morphology of the spreading droplets, we measure the Hausdorff dimension $D \equiv \lim_{r \rightarrow 0} \frac{\log N(r)}{\log 1/r}$ using a box-counting algorithm [25], where r is the box size, and N is the number of boxes necessary to cover the area. As the droplet spreads, D asymptotically approaches a value of 1.30 ± 0.05 at its maximum area (immediately before droplet breakup), as shown by the solid line in Fig. 1b. The same value is observed for all droplet volumes (see Fig. 1b), where the value of \mathcal{E} is selected to provide the largest possible A for that droplet volume. This value of D indicates that this new fingering phenomenon belongs to a different universality class than diffusion-limited aggregation [4], radial viscous fingering in Hele-Shaw cells [26], electrolytic metal deposition [27], directional solidification [28], and dielectric breakdown [13], all of which have fractal dimensions close to 1.7.

Four regimes: Across the range of (\mathcal{E}, V) values tested, we observe four distinct regimes, which we designate as A-D, in an order that corresponds with increasing \mathcal{E} . This order also corresponds to increasing oxide thickness [22, and Supp. Mat.]. Fig. 2 shows representative images of each regime, defined by the main distinguishing features of the droplet shape: smooth (A,D), branched (B), or undulated (C).

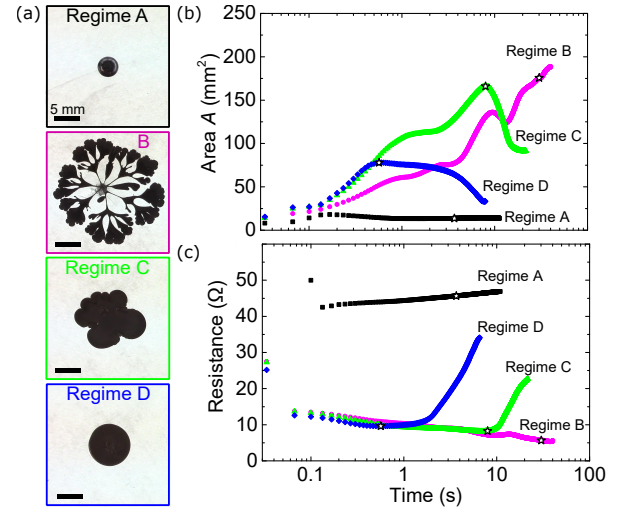


FIG. 2: (a) Representative images taken at the maximum area for all four regimes, and their dynamics characterized by (b) area $A(t)$ and (c) the electrical resistance measured from $(\mathcal{E}/I(t))$. The star indicates the time at maximum area. All panels show data from the same 4 trials with $V = 30 \mu\text{L}$ and $\mathcal{E} = 0.8 \text{ V}$ (Regime A); $\mathcal{E} = 1.8 \text{ V}$ (Regime B); $\mathcal{E} = 2.8 \text{ V}$ (Regime C); and $\mathcal{E} = 4.0 \text{ V}$ (Regime D). The run-to-run variations in area A are $\pm 0.07, 12.7, 26.5,$ and 2.12 mm^2 for regimes A, B, C, and D, respectively.

Whether spreading and/or subsequent contraction occur (see Fig. 2b) also distinguishes the regimes. Note that the droplet volume V is conserved: any increases in area A are accompanied by a decrease in mean droplet height ($h(t) \equiv V/A(t)$), with actual height exhibiting a gradient with h larger in the center.

Regime A ($0.2 \text{ V} < \mathcal{E} < 0.8 \text{ V}$) has been previously studied [22], and is characterized by smooth sessile droplets that remain shiny in appearance. When mechanically perturbed, a droplet in this regime returns to its equilibrium shape. The sessile shape represents a balance between spreading forces (gravity) and restoring forces (interfacial tension). The gravitational force per unit area on the outer rim region is

$$P_g \approx \rho gh \quad (1)$$

and the Laplace pressure (restoring force) is

$$P_L \approx -\frac{2\gamma}{h} \quad (2)$$

where γ is the interfacial tension and $h/2$ is the radius of curvature at the leading edge.

Within Regime A, the droplet reaches an equilibrium shape determined by $P_g + P_L = 0$ (balancing Eq. 1 against 2). Using values of h estimated from A , we calculate that typical pressures decrease from ~ 300 to 50 Pa as \mathcal{E} increases. Since the associated decrease in γ exceeds what can be achieved by electrocapillarity, we attribute it to surface oxidation [19]. Surface oxides are known to lower the interfacial tension of liquid metals, even outside of electrochemical environments [29].

As \mathcal{E} increases above approximately 0.8 V [19, 22], the oxidation lowers γ (and therefore P_L) to the point where an equilibrium shape is no longer possible, and the droplet spreads from a spherical cap into a flatter disk. As the disk spreads it becomes unstable to undulations along its perimeter; this is Regime B. These undulations simultaneously become deeper (extending back to the center electrode) and develop secondary, tertiary, etc. undulations of their own. These dynamics are reminiscent of Marangoni instabilities [8, 9], and can likely also be attributed to local gradients in surface stress. Note that the number of central branches is consistent across all droplet volumes, suggesting the instability is not driven by a fastest-growing wavenumber. The resulting fractal morphology characterized in Fig. 1 shows spreading of approximately $20\times$ the initial area of the droplet. The droplet surface becomes less shiny during this process, particularly around the droplet perimeter, indicating the presence of a rough surface oxide. From the estimated values of h and Eq. 1, we find $P_g \lesssim 1$ Pa once the fractal is well-developed. Balanced against Eq. 2, this implies a conservative upper bound $\gamma \lesssim 0.4$ mN/m. The low interfacial tension is also evidenced by the shape of the branches and undulations, which exhibit both positive and negative radii of curvature.

At larger values of \mathcal{E} , the droplet eventually grows a thicker oxide layer, which halts both the spreading and the development of the undulations; this is Regime C. Instead of branching into a fractal, the droplet *contracts* after about 10 seconds of initial spreading and undulating (Fig. 2b). At still higher values of \mathcal{E} , the oxide growth is sufficiently rapid that the metal stops spreading before any undulations develop; this is Regime D and also exhibits the surprising contraction.

The areal contraction of the metal in Regimes C and D provides a key insight into the fractal fingering observed in Regime B. The instabilities in Regime B are only possible for $\gamma \rightarrow 0$. Yet, in Regimes C and D the retraction is only possible for non-zero γ ; based on the height of the retracted droplets ($h \approx 0.05 - 0.1$ mm), we estimate a lower bound of $\gamma \approx 30$ mN/m. Thus, surface activity of the oxide indeed lowers the tension of the metal (from $\gamma \approx 500$ mN/m in the case of bare metal to as low as $\gamma \approx 30$ mN/m), but this decrease is not sufficient to enable the instabilities in Regime B. After ruling out additional forces such as elasticity, electrostatics, electrostriction, and inertia based on either calculations or ex-

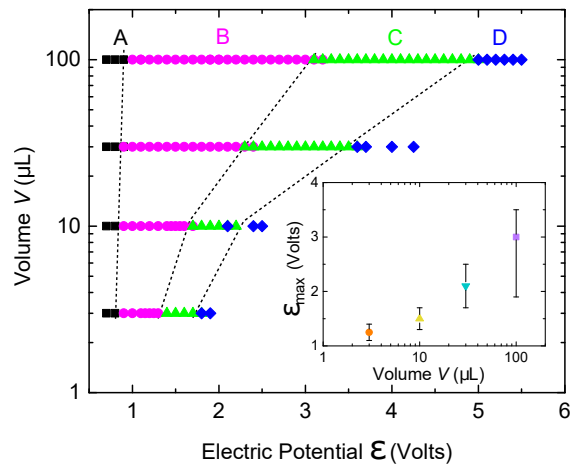


FIG. 3: Phase diagram for droplets of volume V subject to an applied electric potential \mathcal{E} . The dashed black lines correspond to the regime boundaries. Regime A: smooth sessile droplets. Regime B: fractal morphology. Regime C: undulated spreading, followed by contraction. Regime D: spreading followed by contraction. Inset: for each V , the electric potential \mathcal{E}_{\max} at which the maximum spreading extent occurs. Vertical bars represent the width of the $\mathcal{E}(A)$ curves shown in Fig. 4a.

perimental observations (see Supp. Mat.), we determined that oxidative forces help drive instabilities in Regime B.

Previous studies of anodic growth of oxides in aluminum [30] have shown compressive oxidative stresses on the order of 0.1 GPa. Based on the thickness of the oxide (10^{-8} m to 10^{-6} m), this would provide a conservative estimate of a force/length of at least 1 N/m; this force is more than enough to exceed the force provided by the interfacial tension of the metal at this scale (0.1 N/m). Thus, the *effective* interfacial tension is the sum of the surface activity of the fluid (tensile) and the opposing (compressive) stresses from the oxidation process. Qualitatively, such stresses are consistent with the fan-shaped protrusions observed on the surface. We find that the oxide buckles when the liquid metal (under Regime B conditions) is laterally-confined, consistent with the presence of compressive forces. In addition, protrusions form when the droplet is placed in a NaF solution where oxide dissolution does not occur and the oxide should be a mechanical barrier to spreading (see Supp. Mat.)

The electrical measurements provide additional insight into the role of the oxide. In both Regime C and D, the contraction of the droplet corresponds to a rapid increase in electrical resistance ($\Omega \equiv \mathcal{E}/I$, see Fig. 2c). We associate this increase primarily with the thickening oxide layer, consistent with previous impedance [22] and resistance measurements [31]. Consequently, the contribution of the (compressive) oxidative stress to the effective interfacial tension diminishes when the oxide gets too thick. As a result, the droplets contract in Regime C and D due to the non-zero tension of the metal within the oxide. A model of the growth kinetics of the oxide layer, based on measurements of $I(t)$, indicates that the oxide may reach several microns in thickness (see Supp Mat).

Fig. 2c shows that spreading only occurs at low resistance

(i.e. when ions can easily pass through the oxide). Note that the largest values of Ω occur in Regime A. While this might be surprising since the oxide is thinnest for low \mathcal{E} , these are non-ohmic resistances. We find that, within Regime A, the observed values of Ω decrease with droplet volume (consistent with the resistance being dominated by the interface). We speculate that the oxidative stress that drives the fractal instability in Regime B arises because the potential is larger than Regime A, yet the oxide remains thinner than in Regimes C and D (see Supp Mat). Oxidation decreases the system free energy and thus, spreading is present as long as the resistance through the oxide does not provide a sufficient barrier to oxidation.

As a point of clarification, liquid metals have also been observed to migrate towards a counter electrode [32, 33]. While this might suggest the importance of electrostatic forces, our experiments suggest otherwise. Positioning the counter electrode in solution directly above the droplet still results in outward-spreading even though the field lines are largely vertical. In addition, repeating the experiment with a counter electrode ring of half the diameter did not change the behavior of the regimes. However, replacing the circular counter electrode with a point-source placed to the side of the liquid metal caused it to migrate toward the counter electrode. Thus, we surmise, as do [34], that this translational motion is driven by Marangoni forces arising from gradients in tension rather than electrostatic forces. Marangoni forces likely contribute to the growth of the branched structures in Regime B, as evidenced by the eventual breakup of the thin filaments.

Phase diagram: Fig. 3 shows a phase diagram of all experimental runs as a function of (\mathcal{E}, V) , with each symbol representing the characterization of a single run. For each value of V , there is a progression from regime A \rightarrow B \rightarrow C \rightarrow D as \mathcal{E} increases. The phase boundary between Regimes A and B is nearly vertical, as it arises solely from the formation of oxides for $\mathcal{E} > 0.8$ V, independent of V [22]. However, the B/C and C/D boundaries are both tilted in such a way that droplets with a smaller surface-area to volume ratio (larger V) require additional \mathcal{E} to achieve the same transition. This effect is quantified in the inset to Fig. 3, which shows the potential \mathcal{E}_{\max} at which a droplet reaches its maximum area. This observation is consistent with two possible causes: that the Laplace pressure due to the droplet radius R is important for smaller droplets, or that the dynamics of oxide growth and dissolution depend on the surface area.

It is helpful to consider the dimensionless area of the metal $\tilde{A} \equiv A/V^{2/3}$, where droplets with low values of \tilde{A} are more spherical, and high values are more branched. (\tilde{A} is purely a shape parameter, with droplet size scaled out). As shown in Fig. 4a, the maximum value of \tilde{A} is approximately 35 for all droplet volumes; this observation is consistent with the single value of D measured in Fig. 1. This peak value \tilde{A} roughly corresponds to the boundary between Regimes B and C. (Note that in Regime B, the metal continues to spread even after satellite droplets break off; this process is not reflected here.) If the Laplace pressure (Eq. 2) were the dominant effect in controlling the extent of spreading, we would expect that h be

a volume-independent constant at the maximum extent. Since

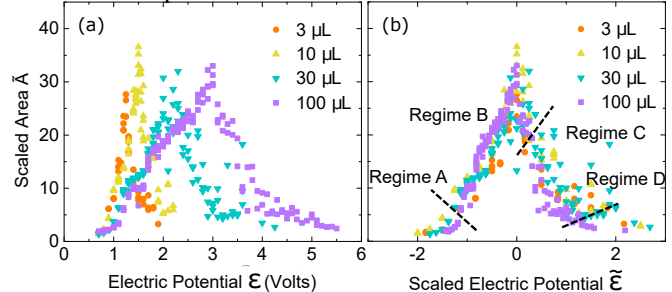


FIG. 4: (a) Scaled area $\tilde{A} \equiv A/V^{2/3}$ as a function of applied electric potential \mathcal{E} . (b) The data from (a) with a rescaled horizontal axis: $(\mathcal{E} - \mathcal{E}_{\max})/\mathcal{E}_w$ to show similarity of results, with $(\mathcal{E}_{\max}, \mathcal{E}_w)$ measured from (a) for each droplet volume.

$V = Ah$, this is not the case, and therefore the Laplace pressure is not the controlling factor. Nonetheless, we find a scaling collapse for $\tilde{A}(\mathcal{E})$ by re-plotting the data as a function of

$$\tilde{\mathcal{E}} = \frac{\mathcal{E} - \mathcal{E}_{\max}}{\mathcal{E}_w} \quad (3)$$

where \mathcal{E}_w is the full width of $A(\mathcal{E})$ at its half-maximum (see Fig. 4b.) This suggests that volume-dependent oxidative rates are an important factor.

Conclusion: Our experiments indicate that surface oxidation lowers the effective interfacial tension and drives instabilities in a gallium-based liquid metal alloy, until the oxide grows too thick and retards further oxidation. This behavior is interesting for a variety of reasons: it shows that an oxide layer can be tuned to both create fingering instabilities and to ultimately halt them; it provides a method to localize and control compressive stresses at a liquid interface using modest potentials; and it has the potential to be used in devices that necessitate shape-reconfigurable conductors. Furthermore, the measured fractal dimension demonstrates a new class of self-similar dynamics and provides a future point of comparison with modeling. Determination of the relevance of local vs. nonlocal effects will be key to this analysis. The ability to alter the shape of a metal in a simple, low-power, and scalable way (e.g. via the hypothesized electrochemically-drive Marangoni effects) could create new types of electronics and actuators, including those that are extremely soft. Future work will focus on quantifying the role of ion-insertion in controlling compressive stresses, including the temporal dynamics and the role of the applied potential.

Acknowledgments: KED is grateful for support under NSF (DMR-1608097) and MDD is grateful for support by NSF (CMMI-0954321) and Air Force Research Lab. KED and MDD acknowledge the NSF Research Triangle MRSEC on Programmable Soft Matter (DMR-1121107). We are grateful to Peter Fedkiw for the loan of a potentiostat, and the NCSU Environmental and Agricultural Testing Service Laboratory for performing the spectroscopy measurements.

-
- [1] P. G. Saffman and G. Taylor, Proceedings of the Royal Society A **245**, 312 (1958).
- [2] T. A. Witten and L. M. Sander, Physical Review Letters **47**, 1400 (1981).
- [3] P. Tabeling, G. Zocchi, and A. Libchaber, Journal of Fluid Mechanics **177**, 67 (1987).
- [4] B. Davidovitch, A. Levermann, and I. Procaccia, Physical Review E **62**, R5919 (2000).
- [5] J. Mathiesen, I. Procaccia, H. L. Swinney, and M. Thrasher, Europhysics Letters **76**, 257 (2006), 0512274.
- [6] J. S. Langer, Reviews of Modern Physics **52**, 1 (1980).
- [7] B. Utter, R. Ragnarsson, and E. Bodenschatz, Physical Review Letters **86**, 4604 (2001).
- [8] S. M. Troian, X. L. Wu, and S. A. Safran, Physical Review Letters **62**, 1496 (1989).
- [9] M. Cachile and A. M. Cazabat, Langmuir **15**, 1515 (1999).
- [10] X. Cheng, L. Xu, A. Patterson, H. M. Jaeger, and S. R. Nagel, Nature Physics **4**, 234 (2008).
- [11] I. Bischofberger, R. Ramachandran, and S. R. Nagel, Nature Communications **5**, 5265 (2014).
- [12] E. Ben-Jacob, O. Schochet, A. Tenenbaum, I. Cohen, A. Czirók, and T. Vicsek, Nature **368**, 46 (1994).
- [13] N. Femia, L. Niemeyer, and V. Tucci, Journal Of Physics D **26**, 619 (1993).
- [14] C. Majidi, R. Kramer, and R. J. Wood, Smart Materials and Structures **20**, 105017 (2011).
- [15] S. Cheng and Z. Wu, Lab on a Chip **12**, 2782 (2012).
- [16] M. D. Dickey, ACS Applied Materials & Interfaces **6**, 18369 (2014).
- [17] S.-Y. Tang, K. Khoshmanesh, V. Sivan, P. Petersen, A. P. O'Mullane, D. Abbott, A. Mitchell, and K. Kalantar-Zadeh, Proceedings of the National Academy of Sciences **111**, 3304 (2014).
- [18] Y. Lu, Q. Hu, Y. Lin, D. B. Pacardo, C. Wang, W. Sun, F. S. Ligler, M. D. Dickey, and Z. Gu, Nature Communications **6**, 10066 (2015).
- [19] C. B. Eaker and M. D. Dickey, Applied Physics Reviews **3**, 031103 (2016).
- [20] M. G. Mohammed and R. Kramer, Advanced Materials p. 1604965 (2017).
- [21] J. T. H. Tsai, C.-M. Ho, F.-C. Wang, and C.-T. Liang, Applied Physics Letters **95**, 251110 (2009).
- [22] M. R. Khan, C. B. Eaker, E. F. Bowden, and M. D. Dickey, Proceedings of the National Academy of Sciences **111**, 14047 (2014).
- [23] J. S. Biggins, Z. Wei, and L. Mahadevan, Europhysics Letters **110**, 34001 (2015).
- [24] M. Zhao, A. Belmonte, S. Li, X. Li, and J. Lowengrub, Journal of Computational and Applied Mathematics **307**, 394 (2016).
- [25] A. Costa, *Hausdorff (box-counting) fractal dimension*, URL <https://www.mathworks.com/matlabcentral/fileexchange/30329-hausdorff--box-counting--fractal-dimension>.
- [26] G. Daccord, J. Nittmann, and H. E. Stanley, Physical Review Letters **56**, 336 (1986).
- [27] Y. Sawada, A. Dougherty, and J. P. Gollub, Physical Review Letters **56**, 1260 (1986).
- [28] A. L. Genau, A. C. Freedman, and L. Ratke, Journal of Crystal Growth **363**, 49 (2013).
- [29] D. Giuranno, E. Ricci, E. Arato, and P. Costa, Acta Materialia **54**, 2625 (2006).
- [30] O. O. Capraz, P. Shrotriya, and K. R. Hebert, Journal of the Electrochemical Society **161**, D256 (2014).
- [31] J.-H. So, H.-J. Koo, M. D. Dickey, and O. D. Velev, Advanced Functional Materials **22**, 625 (2012).
- [32] R. C. Gough, J. H. Dang, M. R. Moorefield, G. B. Zhang, L. H. Hihara, W. A. Shiroma, and A. T. Ohta, ACS Applied Materials & Interfaces **8**, 6 (2016).
- [33] S.-Y. Tang, V. Sivan, K. Khoshmanesh, A. P. O'Mullane, X. Tang, B. Gol, N. Eshtiaghi, F. Lieder, P. Petersen, A. Mitchell, et al., Nanoscale **5**, 5949 (2013).
- [34] S.-C. Tan, X. Yang, H. Gui, Y. Ding, L. Wang, B. Yuan, and J. Liu, Soft Matter **13**, 2309 (2017).
- [35] M. D. Dickey, R. C. Chiechi, R. J. Larsen, E. A. Weiss, D. A. Weitz, and G. M. Whitesides, Advanced Functional Materials pp. 1097–1104 (2008).